Chinese Chemical Letters 37 (2026) 111011

Contents lists available at ScienceDirect

Chinese Chemical Letters

journal homepage: www.elsevier.com/locate/cclet

Design of rare earth borate short-wave UV nonlinear optical crystals with strengthened second harmonic generation activities *via* cationic modification strategy

Huijian Zhao[a,1], Jie Song[a,1], Shuaifeng Li[a], Xianghao Kong[a], Conggang Li[a,*], Ning Ye[a], Zhanggui Hu[a,b,*]

[a] State Key Laboratory of Crystal Materials, Tianjin Key Laboratory of Functional Crystal Materials, Institute of Functional Crystals, Tianjin University of Technology, Tianjin 300384, China
[b] College of Material Science and Engineering, Hefei University of Technology, Hefei 230009, China

ARTICLE INFO

Article history:
Received 30 December 2024
Revised 15 February 2025
Accepted 26 February 2025
Available online 27 February 2025

Keywords:
Rare-earth borates
Second harmonic generation
Chemical substitution strategy
Microscopic polarizability
UV nonlinear optical crystals

ABSTRACT

Ultraviolet (UV) nonlinear optical (NLO) crystals have received substantial interest in advanced laser technology. However, tailoring a UV NLO material with a large second harmonic generation (SHG) response and good UV transparency remains a challenge. Here, inspired by the classic A_3-RE_2-$[BO_3]_3$ parent template, two new rare-earth borate NLO crystals, $RbNa_2La_2(BO_3)_3$ (RNLBO-I) and $Rb_{0.681}Na_{2.319}La_2(BO_3)_3$ (RNLBO-II), were extracted by merging larger ionic radius cations Rb^+ and La^{3+} simultaneously using a chemical substitution-oriented strategy. As expected, both compounds achieve significant enhancements in SHG activities, reaching 4.5 × and 4.3 × KDP, respectively, exceeding three times that of the isomorphic $Na_3Gd_2B_3O_9$. Notably, RNLBO-I displayed the highest SHG response among alkali metal RE-borate NLO crystals containing isolated $[BO_3]$ groups in the short-wave UV region. Moreover, RNLBO-I and -II demonstrated short UV cutoff edges at 213 and 207 nm, corresponding to wide bandgaps of 5.3 and 5.6 eV, respectively. Additionally, theoretical calculations and dipole moment analysis were conducted to clarify the origin of the enhanced SHG activities of RNLBO-I and -II. The optimal balance between SHG intensity and UV transparency in RNLBO-I and -II underscores their potential as UV NLO candidates and offers valuable insights for fabricating new advanced UV NLO materials.

© 2026 Published by Elsevier B.V. on behalf of Chinese Chemical Society and Institute of Materia Medica, Chinese Academy of Medical Sciences.

Ultraviolet (UV) coherent lights sources, characterized by high photon energy and spatial resolution, have attracted increasing interest for their applications in optoelectronic fields including microelectronics fabrication and semiconductor inspections [1–4]. The development of UV coherent light sources, limited by the emitted laser wavelengths of all-solid-state lasers, necessitates the exploration of nonlinear optical (NLO) crystals capable of extending the coherent light wavelength into the UV region [5–11]. Over the decades, significant efforts are being directed toward the design and fabrication of innovative NLO crystals. The discovery of commercially available UV NLO materials, such as β-BaB_2O_4 (BBO) [12], LiB_3O_5 (LBO) [13], and KBBF ($KBe_2BO_3F_2$) [14] has been facilitated by elucidating the structure-property relationship based on the anionic group theory proposed by Chen [15]. In general, noteworthy characteristics of UV NLO crystals include strong second harmonic generation (SHG) and a wide UV transmission range; however, the inherent trade-off between these indicators presents a considerable challenge in the development of short-wave UV NLO crystals.

The performance of NLO crystals is primarily governed by the geometry of fundamental building blocks (FBBs) and distinct spatial arrangement, as exemplified by anionic groups featuring a π-conjugated system and second-order Jahn–Teller (SOJT) active cations [16–20]. The strategic incorporation of these components enhances the likelihood of forming acentric structures, which are essential for achieving desirable NLO properties. A promising approach for identifying high-performing UV NLO materials involves a chemical substitution-oriented strategy, wherein one or more FBBs, cations, or anions in a prototype structure are replaced to tailor their properties [21]. For instance, utilizing the classic KBBF as a parent structure, a beryllium-free borate, $Li_4Sr(BO_3)_2$, was developed by substituting the $[Be_2BO_3F_2]_\infty$ layers with $[SrBO_3]_\infty$ anionic layers, resulting in improved layering tendencies and SHG efficiency (1.5 × KBBF) [22]. Similarly, Yu *et al.* replaced Be^{2+}

* Corresponding authors.
E-mail addresses: cgli@email.tjut.edu.cn (C. Li), hu@mail.ipc.ac.cn (Z. Hu).
[1] These authors contributed equally to this work.

https://doi.org/10.1016/j.cclet.2025.111011
1001-8417/© 2026 Published by Elsevier B.V. on behalf of Chinese Chemical Society and Institute of Materia Medica, Chinese Academy of Medical Sciences.

with Zn^{2+} cations in the KBBF structure while introducing halogen anions, yielding KBBF-like crystals, $CsZn_2BO_3X_2$ (X = F, Cl), which exhibited enhanced SHG responses of 2.8–3.5 times that of KDP [23]. Furthermore, the deep-UV NLO crystal $Li_2B_6O_9F_2$ [24], was identified by replacing [BO] motifs in LBO with [BOF] fluorooxoborate groups. Additionally, acentric isomorphic compounds $A_3VO(O_2)_2CO_3$ were developed through a single-site substitution method, where SHG responses increased with the enlarged size of the alkali metal cation (A = K, Rb, Cs) [25–27]. This indicates that the strategic substitution of FBBs and cations in a prototype phase can significantly facilitate the discovery of new UV NLO materials.

Rare earth (RE)-based borates are promising sources for exploiting UV NLO crystals owing to their versatile chemical frameworks that facilitate the formation of acentric structures. Herein, we utilize the classic A_3-RE_2-$[BO_3]_3$ (A = alkali metal) parent template [28,29], aiming to substitute the RE^{3+} and A^+ cations with larger ionic radii to develop new RE-based borate UV NLO crystals. The $[BO_3]$ groups, characterized by conjugated π-orbitals and highly anisotropic electron distributions, serve as preferred FBBs due to their significant microscopic second-order susceptibilities [30–36]. Besides, the RE cation La^{3+} with closed-shell electronic configurations, effectively suppresses unwanted d−d or f–f electronic transitions, thereby widening the bandgap [33,34]. The introduction of the larger ionic radius cation Rb^+, not only strengthens interatomic interactions with adjacent O atoms but also results in a blue shift of the absorption edge. Systematic explorations of the A_3-RE_2-$[BO_3]_3$ system led to the discovery of two new RE-borate NLO crystals, $RbNa_2La_2(BO_3)_3$ (RNLBO-I) and $Rb_{0.681}Na_{2.319}La_2(BO_{3)3}$ (RNLBO-II) *via* a chemical substitution strategy. Structural analysis revealed that the Rb^+ cations exert an influence on the geometry and increase the dipole moment of the $[BO_3]$ planar triangle in RNLBO-I and -II, compared to those in $Na_3Gd_2B_3O_9$. As expected, RNLBO-I and -II exhibit strong SHG intensities of 4.5 × and 4.3 × KDP, respectively, which enhance their SHG efficiencies to three times that of the isomorphic template $Na_3Gd_2B_3O_9$ (1.3 × KDP) [29]. Notably, RNLBO-I demonstrates the highest SHG response among the RE-borate NLO crystals containing isolated $[BO_3]$ motif in the short-wave UV window ($\lambda_{cutoff} \leq 266$ nm). Moreover, both compounds displayed short UV cutoff edges of 213 and 207 nm, corresponding to wide bandgaps of 5.3 and 5.6 eV, respectively. The balanced coexistence of desirable SHG activity and broad UV transparency range underscores the potential of RNLBO-I and -II as promising candidates for short-wave UV NLO applications.

Polycrystalline RNLBO-I and RNLBO-II were synthesized *via* high-temperature solid-state reaction. As shown in Fig. 1a, the PXRD patterns obtained from the experiment match well with the results derived from theoretical calculations, respectively, providing strong evidence for the synthesis of pure-phase RNLBO-I and RNLBO-II compounds. The tiny peak observed at 25.5° can be attributed to the centrosymmetric phase of the $LaBO_3$ impurity. More intuitively, the enlarged PXRD curves presented in Fig. 1b highlight the distinct PXRD peaks observed in RNLBO-I at 23.1°, 26.3°, and 33.8° corresponding to the (120), (031), and (122) facets, respectively. Likewise, in RNLBO-II, the peaks observed around 23.3°, 26.6°, and 34.1° for the respective facets, respectively. Notably, the shift of PXRD peaks towards lower angles with the increasing Rb^+ cation ratio, which signifies the evolving composition in both RNLBO-I and RNLBO-II, corroborating the distinctions in cell parameters between the two compounds. Moreover, we conducted TG-DSC analysis to assess the thermal behavior of both compounds, as demonstrated in Figs. 1c and d. The observed curves showcase the thermal response of RNLBO-I and RNLBO-II across a temperature range ranging from 50 °C to 1200 °C. Noticeably, distinct endothermic peaks are observed at approximately 1066 °C for RNLBO-I and 1111 °C for RNLBO-II, whereas the corresponding TG

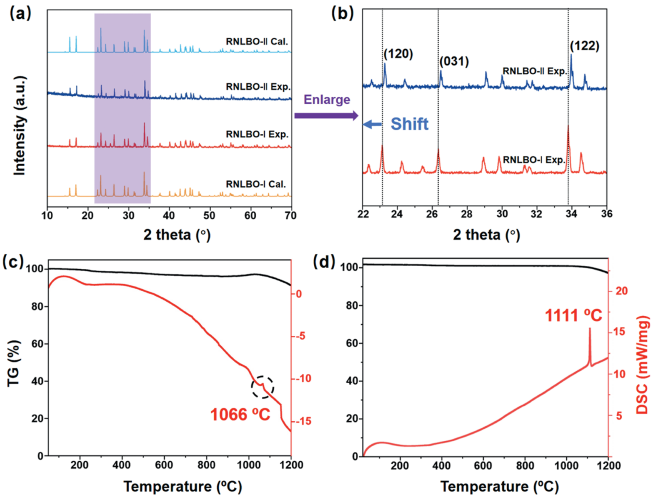


Fig. 1. (a, b) Experimental and calculated PXRD patterns, along with enlarged PXRD curves observed in the 2θ range of 22°–36° for the polycrystalline samples of RNLBO-I and RNLBO-II, respectively. (c, d) TG-DSC curves for the RNLBO-I and RNLBO-II compounds, respectively.

curves exhibit minimal weight loss, signifying the exceptional thermal stability of RNLBO-I and RNLBO-II.

Two isostructural compounds, RNLBO-I and RNLBO-II, were identified using a chemical substitution-oriented strategy. Given the structural similarity between RNLBO-I and RNLBO-II (Fig. S1 in Supporting information), RNLBO-I was chosen as the representative sample for thorough structural analysis. The crystal structure of RNLBO-I was fully characterized through single crystal XRD, revealing its classification under the orthorhombic space group *Amm*2 (No. 38). The unit cell parameters were determined to be $a = 5.2036(18)$ Å, $b = 11.4185(4)$ Å, $c = 7.3175(3)$ Å, with a corresponding volume of $V = 434.79(3)$ Å^3. Extensive structural analysis of RNLBO-I is provided in Table S1 (Supporting information). The asymmetric unit of RNLBO-I contains two types of B atoms, one La atom, one independent Rb atom, two independent Na atoms, and two distinct O atoms. Further information regarding bond lengths is listed in Table S2 (Supporting information), revealing the B-O bond distances ranging from 1.356 Å to 1.440 Å, and La-O bond lengths varying between 2.457 Å and 2.956 Å. As shown in Fig. 2a, one B atom coordinates with three O atoms to form a $[BO_3]$ plane triangle, with these triangles existing independently in space, while the La atom forms a relatively distorted $[LaO_9]$ polyhedron bonded to nine oxygen atoms. These adjacent $[LaO_9]$ polyhedra are interconnected through edge-sharing oxygen atoms to form a $[La_2O_{16}]_\infty$ *pseudo*-one-dimensional (1D) chain. These chains are further linked with the $[BO_3]$ units through corner-sharing oxygen atoms, constructing a *pseudo*-two-dimensional (2D) layer parallel to the *bc* plane (Fig. 2b). Subsequently, the *pseudo*-2D layers are further bridged by $[BO_3]$ units, creating a three-dimensional (3D) structural framework viewed along the *c*-axis (Fig. 2c), with alkali metal cations Na^+ and Rb^+ located between these layers to balance the overall charge (Fig. 2d). Additionally, bond valence calculations of RNLBO-I were carried out, revealing the oxidation states of Rb, Na, La, B and O atoms to parallel to the expected values of +1, +1, +3, +3, and −2, respectively (Table S4 in Supporting information).

The crystal structure of RNLBO-I displays resemblances to the isostructural $Na_3La_2(BO_3)_3$ and $KNa_2La_2(BO_3)_3$ [28,33], featuring a consistent arrangement of $[BO_3]$ planar triangles and distorted $[LaO_9]$ polyhedra. Nevertheless, a notable distinction arises in the unique interconnection of A-position cations Rb^+ and Na^+ in both compounds. As shown in Fig. S2a (Supporting information), the

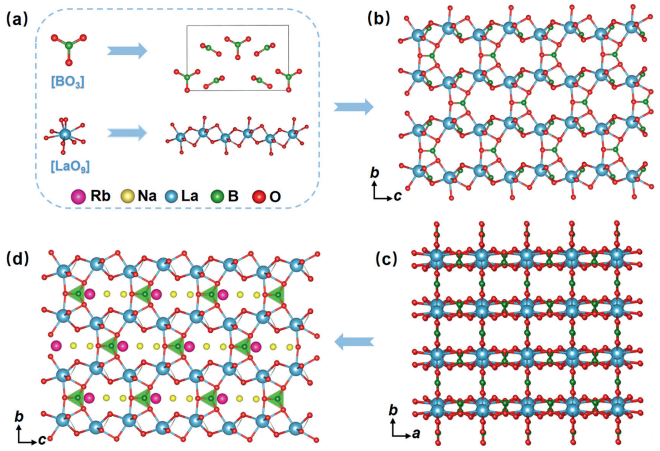


Fig. 2. Structural characteristics of RNLBO-I. (a) $[BO_3]$ planar triangles, $[LaO_9]$ polyhedra, and $[La_2O_{16}]_\infty$ clusters. (b) The presentation of connection between the $[BO_3]$ and $[LaO_9]$ groups *via* corner-sharing along the *bc* plane. (c, d) 3D structural network viewed along the *c*- and *a*-axis, respectively.

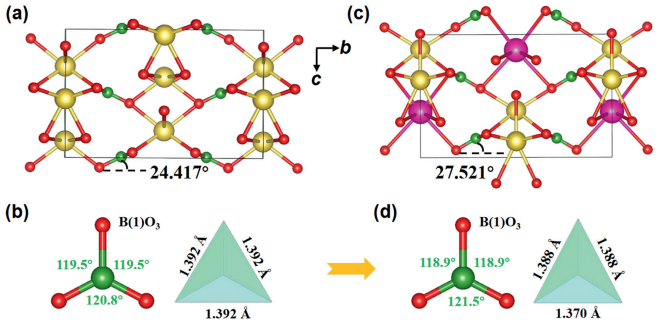


Fig. 3. (a) The 3D structural network of $Na_3La_2(BO_3)_3$ observed along the *a*-axis. (b) The bond lengths and bond angles of the $[B(1)O_3]$ in $Na_3La_2(BO_3)_3$. (c) The 3D structure network of RNLBO-I observed along the *a*-axis. (d) The bond lengths and bond angles of the $[B(1)O_3]$ units in RNLBO-I.

incorporation of Rb^+ with a larger ionic radius exerts an impact on the configuration and spatial arrangement of the $[BO_3]$ triangles. In $Na_3La_2(BO_3)_3$, Na atoms coordinate with six and eight O atoms to form $[NaO_6]$ and $[NaO_8]$ polyhedra, respectively. Conversely, in RNLBO-I, Rb and Na atoms coordinate with various O atoms to generate $[RbO_{10}]$, $[NaO_7]$, and $[NaO_8]$ polyhedra, respectively, presented in Fig. S2b (Supporting information). Furthermore, the adjacent $[NaO_6]$ and $[NaO_8]$ polyhedra are interconnected to form *pseudo*-1D $[Na_4O_{18}]_\infty$ chains along the *c*-axis in $Na_3La_2(BO_3)_3$ (Fig. S2c in Supporting information), whereas the interconnection of one $[RbO_{10}]$, one $[NaO_7]$, and one $[NaO_8]$ polyhedra generates *pseudo*-1D $[RbNa_3O_{18}]_\infty$ chains along the *c*-axis in RNLBO-I (Fig. S2d in Supporting information). The distinct coordination modes exhibited by the A-site alkali metal cations influence the configuration of $[BO_3]$ in $Na_3La_2(BO_3)_3$ and RNLBO-I. As demonstrated in Fig. 3a, in $Na_3La_2(BO_3)_3$, the angle between the plane containing the $[B(1)O_3]$ group and the *ab* plane measures 24.417°, and the corresponding $[B(1)O_3]$ primitive approximates an equilateral triangle (Fig. 3b). In contrast, this angle increases to 27.521° in RNLBO-I (Fig. 3c), and its corresponding $[B(1)O_3]$ unit is approximately an isosceles triangle (Fig. 3d). Accordingly, this variation indicates that the $[B(1)O_3]$ units in RNLBO-I could possess higher microscopic polarizability compared to $Na_3La_2(BO_3)_3$, which significantly contributes to the NLO properties of the material.

Spectroscopic properties of both compounds were examined to gain insights into their optical behavior. As shown in Figs. 4a and b, the UV–vis-NIR diffuse reflectance spectra revealed that the UV absorption cutoff edges for RNLBO-I and RNLBO-II are determined to be 213 and 207 nm, respectively, comparable to the isomorphic compounds $Na_3La_2(BO_3)_3$ and $KNa_2La_2(BO_3)_3$ [28,33]. Employing the Kubelka-Munk equation [35], the corresponding experimental bandgaps were found to be 5.3 and 5.6 eV, respectively. Additionally, IR spectroscopy measurements were conducted over a range between 2000 cm^{-1} and 400 cm^{-1} on the title compounds. As displayed in Fig. 4c, the characteristic absorption peak observed at 1193 cm^{-1} primarily corresponds to the asymmetric stretching vibration of $[BO_3]$ units. The absorption peaks at around 744, 662, and 586 cm^{-1} are mainly associated with the out-of-plane bending and in-plane bending vibrations induced by $[BO_3]$ units [36–38]. These infrared spectral features further verify the configuration of

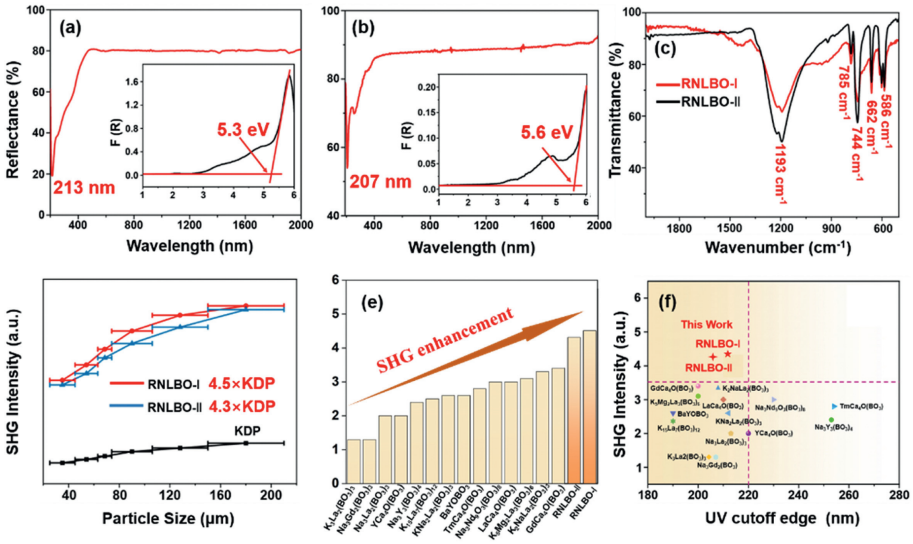


Fig. 4. Optical characterization of RNLBO-I and RNLBO-II. (a, b) UV–vis-NIR diffuse reflectance spectra and corresponding bandgaps for RNLBO-I and RNLBO-II, respectively. (c) IR spectrum for the RNLBO-I and RNLBO-II polycrystalline, respectively. (d) Phase-matched curves and SHG intensities for KDP, RNLBO-I, and RNLBO-II, respectively, under 1064 nm laser radiation. (e) Comparison of the reported SHG intensity of alkali/alkaline earth metal RE borates containing $[BO_3]$ units. (f) Scatter diagrams of SHG intensity and UV cutoff edges of alkali/alkaline earth metal RE borates containing isolated $[BO_3]$ units.

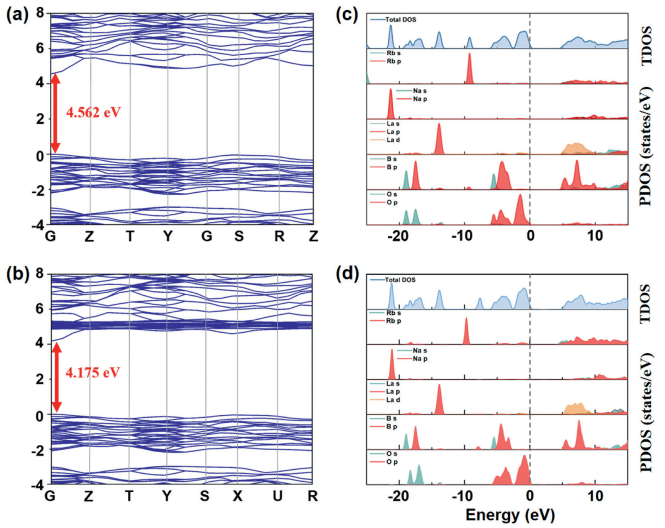


Fig. 5. (a, b) Calculated band structures of RNLBO-I and RNLBO-II, respectively. (c, d) Total and partial densities of states (TDOS and PDOS) of RNLBO-I and RNLBO-II, respectively.In conclusion, we have successfully synthesized two novel alkali metal rare earth borates, RNLBO-I and RNLBO-II, utilizing a chemical substitution-oriented approach. Both compounds adopt the acentric space group *Amm*2 (No. 38), showcasing a distinct 3D structural network composed of planar triangular units [BO_3] and distortive polyhedra [LaO_9]. Notably, RNLBO-I and RNLBO-II achieve an ideal balance between strong SHG effects (4.5 × and 4.3 × KDP) and short UV cutoff edges (213 and 207 nm). Intriguingly, the excellent SHG behaviors exhibited by RNLBO-I and RNLBO-II demonstrate the highest SHG values among alkali metal RE-borate NLO crystals containing isolated [BO_3] groups in the short-wave UV region ($\lambda_{cutoff} \leq$ 266 nm). Additionally, structural analysis and dipole moment calculations elucidated the origin of the observed SHG activities in both compounds. These findings underscore the potential of RNLBO-I and RNLBO-II as promising short-wave UV NLO crystals and offer a convenient avenue for the design of innovative NLO crystals in the UV wavelength region.

the [BO_3] units in the structures of RNLBO-I and RNLBO-II, which aligns well with the structural data obtained.

Powder SHG measurements were implemented on the title compounds to assess their NLO activities, using KDP samples as a reference. The relationship between powder SHG effects and particle sizes of the title compounds is depicted in Fig. 4d. It is noted that as the particle size increases, the corresponding SHG intensity gradually increases until reaching a saturation point, suggesting the phase-matchable ability of both compounds [39]. Notably, RNLBO-I and RNLBO-II exhibit strong SHG responses that are 4.5 and 4.3 times that of KDP, and 1.13 times that of LBO under 1064 nm radiation (Fig. S3 in Supporting information), respectively, within the particle size range of 177–210 μm. Intriguingly, to our best knowledge, RNLBO-I demonstrates the highest SHG response among alkali/alkaline metal RE-borate NLO crystals containing isolated [BO_3] units in the short-wave UV region (Table S6 in Supporting information, Figs. 4e and f). This desirable observation highlights the potential of the title compounds as promising UV NLO crystals that achieve a desired balance between strong SHG intensity and a wide UV transmission range. Previous studies suggested that the SHG response of borate based NLO crystals is primarily influenced by the π-conjugated B-O units [28,34]. To probe the contribution of structural units to the SHG response, we calculated the dipole moment of the [BO_3] units (Table S7 in Supporting information). The results reveal that the total dipole moment of the [BO_3] units in RNLBO-I and RNLBO-II is 3.41 and 1.49 Debye, respectively, exceeding that of the isostructural $Na_3La_2(BO_3)_3$ (1.11 Debye) [22], consistent with the observed SHG signals. Therefore, it can be concluded that the structural chromophore [BO_3] plays a key role in the SHG-active activity of RNLBO-I and RNLBO-II.

To gain deeper insights into the fundamental factors influencing the optical properties of RNLBO-I and RNLBO-II, electronic structure calculations based on density functional theory (DFT) were employed [40,41]. The analysis of the energy band structure (Figs. 5a and b) revealed that both RNLBO-I and RNLBO-II are direct bandgap materials with calculated bandgaps 4.562 and 4.175 eV, respectively, slightly lower than the experimental results of 5.3 and 5.6 eV. Furthermore, the analysis of total and partial densities of states (TDOS and PDOS) was conducted and presented in Figs. 5c and d. It was observed that in the vicinity of the Fermi level, the top of the valence band within the −5∼0 eV range is mainly contributed by B 2p orbitals, while the bottom of the conduction band spanning 5–10 eV is chiefly composed of La 5d and B 2p orbitals. Given the established principle that the optical behavior of a material is largely associated with its electronic transitions near the Fermi energy, it is inferred that the synergistic interaction of the [BO_3] planar triangles and distorted [LaO_9] polyhedra plays a crucial role in the exhibited NLO activities of RNLBO-I and RNLBO-II. This observation is also consistent with the dipole moment analysis performed on both compounds. Besides, based on the calculated electronic structure, the dispersion curves of the refractive indices of RNLBO-I were evaluated, yielding a theoretical birefringence value of 0.024 at 1064 nm (Fig. S4 in Supporting information). This moderate birefringence is comparable to that of other isostructural RE-earth borate crystals containing [BO_3] units, such as $KNa_2La_2(BO_3)_3$ (0.019@1 μm), $K_2NaYB_2O_6$ (0.028@1064 nm), and $Na_3La_2(BO_3)_3$ (0.023@1064 nm) [28,33,42].

Declaration of competing interest

The authors declare that they have no known competing financial interests or personal relationships that could have appeared to influence the work reported in this paper.

CRediT authorship contribution statement

Huijian Zhao: Writing – original draft, Investigation, Formal analysis, Data curation. **Jie Song:** Software, Investigation, Formal analysis. **Shuaifeng Li:** Software, Formal analysis. **Xianghao Kong:** Software, Formal analysis. **Conggang Li:** Writing – review & editing, Project administration, Methodology, Funding acquisition, Conceptualization. **Ning Ye:** Resources, Funding acquisition. **Zhanggui Hu:** Resources, Funding acquisition.

Acknowledgments

This work was supported by the National Key R&D Program of China (No. 2021YFA0717800), National Natural Science Foundation of China (Nos. 62475191, 61835014, and 52327801).

Supplementary materials

Supplementary material associated with this article can be found, in the online version, at doi:10.1016/j.cclet.2025.111011.

References

[1] P. Halasyamani, J. Rondinelli, Nat. Commun. 9 (2018) 2972.
[2] Y. Yang, X. Liu, C. Zhu, et al., Angew. Chem. Int. Ed. 62 (2023) e202301404.
[3] X. Jiang, M. Zhang, H. Zeng, et al., J. Am. Chem. Soc. 133 (2011) 3410–3418.
[4] C. Pan, X. Yang, L. Xiong, et al., J. Am. Chem. Soc. 142 (2020) 6423–6431.
[5] M. Xia, X. Jiang, Z. Lin, et al., J. Am. Chem. Soc. 138 (2016) 14190–14193.
[6] X. Dong, H. Huang, L. Huang, et al., Angew. Chem. Int. Ed. 63 (2024) e202318976.
[7] K. Wu, B. Zhang, Z. Yang, et al., J. Am. Chem. Soc. 139 (2017) 14885–14888.
[8] F. Liang, L. Kang, P. Gong, et al., Chem. Mater. 29 (2017) 7098–7102.
[9] M. Wu, E. Tikhonov, A. Tudi, et al., Adv. Mater. 35 (2023) 2300848.
[10] B. Zhang, E. Tikhonov, C. Xie, et al., Angew. Chem. Int. Ed. 58 (2019) 11726–11730.

[11] C. Wu, C. Jiang, G. Wei, et al., J. Am. Chem. Soc. 145 (2023) 3040–3046.
[12] K. Miyazaki, H. Sakai, T. Sato, Opt. Lett. 11 (1986) 797–799.
[13] C. Chen, Y. Wu, A. Jiang, et al., J. Opt. Soc. Am. B 6 (1989) 616–621.
[14] B. Wu, D. Tang, N. Ye, et al., Opt. Mater. 5 (1996) 105–109.
[15] W. Wang, D. Mei, S. Wen, et al., Chin. Chem. Lett. 33 (2022) 2301–2315.
[16] M. Mutailipu, M. Zhang, H. Wu, et al., Nat. Commun. 9 (2018) 3089.
[17] M. Mutailipu, K. Poeppelmeier, S. Pan, Chem. Rev. 121 (2021) 1130–1202.
[18] H. Liu, H. Wu, Z. Hu, et al., J. Am. Chem. Soc. 145 (2023) 12691–12700.
[19] H. Yu, W. Zhang, J. Young, et al., J. Am. Chem. Soc. 138 (2016) 88–91.
[20] L. Gao, Y. Han, C. Lin, et al., Chin. Chem. Lett. 35 (2024) 109529.
[21] G. Zou, K. Ok, Chem. Sci. 11 (2020) 5404–5409.
[22] S. Zhao, P. Gong, L. Bai, et al., Nat. Commun. 5 (2014) 4019.
[23] J. Zhou, Y. Liu, H. Wu, et al., Angew. Chem. Int. Ed. 59 (2020) 19006–19010.
[24] B. Zhang, G. Shi, Z. Yang, et al., Angew. Chem. Int. Ed. 56 (2017) 3916–3919.
[25] G. Zou, Z. Lin, H. Zeng, et al., Chem. Sci. 9 (2018) 8957–8961.
[26] G. Zou, H. Jo, S. Lim, et al., Angew. Chem. Int. Ed. 57 (2018) 8619–8622.
[27] Y. Song, M. Luo, F. Liang, et al., Chem. Commun. 54 (2018) 1445–1448.
[28] G. Zhang, Y. Wu, P. Fu, et al., Chem. Lett. 30 (2001) 456–457.
[29] W. Zhou, R. Zhuang, W. Zhao, et al., Cryst. Res. Technol. 46 (2011) 926–930.
[30] Y. Liu, X. Liu, S. Liu, et al., Angew. Chem. Int. Ed. 59 (2020) 7793–7796.
[31] G. Peng, C. Lin, H. Fan, et al., Angew. Chem. Int. Ed. 60 (2021) 17415–17418.
[32] M. Luo, F. Liang, Y. Song, et al., J. Am. Chem. Soc. 140 (2018) 6814–6817.
[33] J. Song, C. Li, J. Jiao, et al., Inorg. Chem. Front. 10 (2023) 5488–5495.
[34] J. Song, H. Zhao, C. Li, et al., Chem. Sci. 15 (2024) 16196–16204.
[35] P. Kubelka, F. Munk, Z. Tech. Phys. 12 (1931) 259–274.
[36] J. Song, C. Hu, X. Xu, et al., Angew. Chem. Int. Ed. 54 (2015) 3679–3682.
[37] J. Liu, Y. Chen, M. Sun, et al., Cryst. Growth Des. 24 (2024) 2343–2348.
[38] X. Long, R. An, Y. Lv, et al., Chem. Eur. J. 30 (2024) e202401488.
[39] S. Kurtz, T. Perry, J. Appl. Phys. 39 (1968) 3798–3813.
[40] R. Godby, M. Schlüter, L. Sham, Phys. Rev. B 37 (1988) 10159–10175.
[41] S. Clark, M. Segall, C. Pickard, et al., Z. Kristallogr. 220 (2005) 567–570.
[42] J. Song, X. Kong, C. Li, et al., Inorg. Chem. 63 (2024) 14786–14793.